



HAL
open science

A novel intelligent RISE feedback control of autonomous tethered underwater vehicles: Design & real-time experiments

Raissa Benazouz, Ahmed Chemori, Vincent Creuze

► To cite this version:

Raissa Benazouz, Ahmed Chemori, Vincent Creuze. A novel intelligent RISE feedback control of autonomous tethered underwater vehicles: Design & real-time experiments. *Ocean Engineering*, 2024, 300, pp.117470. 10.1016/j.oceaneng.2024.117470 . lirmm-04507735

HAL Id: lirmm-04507735

<https://hal-lirmm.ccsd.cnrs.fr/lirmm-04507735v1>

Submitted on 17 Mar 2024

HAL is a multi-disciplinary open access archive for the deposit and dissemination of scientific research documents, whether they are published or not. The documents may come from teaching and research institutions in France or abroad, or from public or private research centers.

L'archive ouverte pluridisciplinaire **HAL**, est destinée au dépôt et à la diffusion de documents scientifiques de niveau recherche, publiés ou non, émanant des établissements d'enseignement et de recherche français ou étrangers, des laboratoires publics ou privés.

A novel intelligent RISE feedback control of autonomous tethered underwater vehicles: Design & real-time experiments

Raissa Benazouz^a, Ahmed Chemori^{a,*} and Vincent Creuze^a

^aLIRMM, University of Montpellier, CNRS, Montpellier, France

ARTICLE INFO

Keywords:
RISE Feedback control
Underwater vehicles
Fuzzy logic control
Real-time experiments
Robustness.

ABSTRACT

This paper deals with the tracking control problem of small autonomous tethered underwater vehicles. It proposes a new extended robust integral of the sign of the error (RISE) feedback control. The proposed RISE-based extension benefits from a fuzzy inference system to automatically and online tune the parameters of the RISE controller. The resulting intelligent control scheme is named Fuzzy RISE (FRISE) feedback control. Several real-time experimental scenarios, in different operating conditions, were conducted on Leonard underwater vehicle to demonstrate the efficiency and robustness of the proposed control scheme. It was also compared with some existing controllers from the literature to show its performances.

1. Introduction and related work

The underwater environment covers approximately 71% of the earth surface and supports approximately 90% of all life forms, making it a strategic and resource-based environment with great potential benefits for human life [1]. However, accessing the deeper floors of the ocean presents significant challenges, including poor visibility, extreme pressure, low temperature, and unstructured topography, which induce safety risks to humans and conventional manned vehicles (submarines) [2]. To overcome these challenges, researchers have proposed using unmanned underwater vehicles/robots (UUVs) equipped with intelligent capabilities to explore and exploit underwater environments. In recent years, the use of UUVs has become increasingly common due to their performance and flexibility in various fields such as military, commercial, and scientific research applications [3]. They are a viable alternative for carrying out tasks that are impossible for humans due to potential safety issues. The advancements in UUVs have revolutionized the exploration and exploitation of the underwater environment, leading to significant progress in deep ocean areas and the activities of maritime industries [4].

Despite the significant advancements in UUVs technology [5] several challenges persist during underwater missions, such as communication, perception, sensing, reliable autonomy, and control. To perform tasks efficiently, UUVs require autonomy in positioning the vehicle or tracking a predefined trajectory for mapping an area of interest, making control one of the most challenging requirements [6]. Therefore, researchers have proposed various control techniques in recent years to address these challenges and improve the performance of UUVs.

One of the widely used control schemes is classical control schemes, which includes PD/PID controllers and


their variants [7],[8]. These controllers are simple to implement but lack robustness against uncertainties and external disturbances [9]. Robust control schemes like sliding mode controllers [10], fuzzy logic controllers [11], [12], neural network controllers [13], and adaptive techniques [14], [15] have been proposed to overcome this limitation and provide better performances. Hybrid intelligent controllers combining multiple control schemes have also been proposed [16]. However, these advanced controllers are more challenging to implement and require fine tuning for specific operating conditions. A detailed review of the literature about AUV control is available in [17].

The robust integral of the sign of the error (RISE) [18], is a class of SMC-like techniques that guarantee semi-global asymptotic tracking for nonlinear uncertain systems. Unlike other SMC methods, RISE includes a singular integral signum term that can handle smooth bounded disturbances. Although the robustness of the standard RISE control is one of its main characteristics, this is achieved only at the expense of the introduction of the integral term in the controller; which may grow indefinitely and exceed the mechanical actuator limits in the critical condition of nonlinearities and disturbances [19]. Therefore, different approaches for improving the performance of the standard RISE have been proposed in the literature [20], [21] and [22].

In this study, we propose the design of an intelligent RISE controller that considers this issue. The proposed controller combines a standard RISE controller with a fuzzy logic inference system to dynamically adjust the gains in the aim of improving the trajectory tracking performance. The main contributions of this study can be summarized as follows:

- An enhanced RISE (named intelligent RISE) feedback control is developed to ensure a better robustness towards parametric uncertainties and external disturbances.
- Several real-time experimental scenarios are conducted to demonstrate the efficiency and robustness

*Corresponding author

 raissa.benazouz@lirmm.fr (R. Benazouz); ahmed.chemori@lirmm.fr (A. Chemori); vincent.creuze@lirmm.fr (V. Creuze)

ORCID(s): 0009-0009-9208-1744 (R. Benazouz); 0000-0001-9739-9473 (A. Chemori); 0000-0002-6813-8562 (V. Creuze)

of the proposed intelligent RISE control scheme w.r.t existing controllers, namely a PID and a conventional RISE controller.

2. Vehicle description and modeling

2.1. Vehicle description

The real-time experiments are conducted using one of LIRMM's underwater prototypes, named Leonard, as illustrated in Fig. 1. Leonard is a tethered underwater vehicle, entirely designed and built at LIRMM, part of the University of Montpellier and CNRS, France. Its dimensions are 75cm long, 55cm width, and 45cm height, and it weighs 28kg. Table 1 summarizes some of the vehicle's technical features, as well as its parameters. For more details about the Leonard underwater vehicle, the reader can refer to [15] and [10].



Figure 1: Leonard autonomous underwater vehicle.

The propulsion system of this vehicle consists of six independent propellers Fig. 2, making it a holonomic fully actuated system capable of maintaining stability in its six degrees of freedom (6DOFs). These propellers are controlled by a computer located at the surface via an umbilical cable and are capable of maintaining the vehicle in any desired orientation. The computer is a laptop with an Intel Core i7-3520M 2.9GHz CPU, 8GB of RAM, running under Windows 10 operating system. The control software is developed using Visual C++ language. The laptop receives the data from the underwater vehicle's sensors, computes the control laws, and sends control actions to each thruster of Leonard.

Leonard can be operated either remotely or autonomously, this makes it perfectly suited for a wide range of marine operations. The design of the vehicle ensures that the center of buoyancy and the center of gravity help the robot to remain passively stable in pitch and roll. This feature not only reduces the vehicle's energy consumption but also enables the vehicle to maintain a near-zero roll and pitch with respect to the horizontal plane.

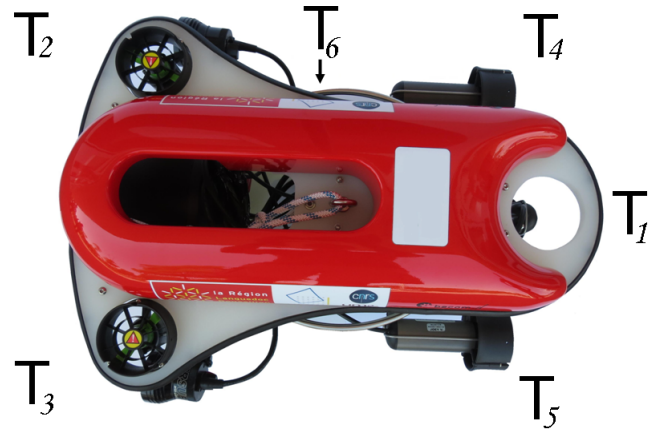


Figure 2: Illustration of the six actuators of Leonard autonomous underwater vehicle as well as their configuration.

Table 1

The main technical features of Leonard UUV.

Hardware components and parameters	Descriptions and their specifications
Attitude Sensor	Sparkfun MPU 9250, MEMS 9-axes gyrometer, accelerometer and magnetometer.
Depth Sensor	Pressure sensor MS5803-02BA.
Dimensions	75cm (Length) × 55cm (Width) × 45cm (Height).
Sampling Periods	40ms (Attitude sensor) and 50ms (Depth sensor).
Floatability	9N.
Mass	28Kg.
Maximal Depth	100m (range also depending on the depth sensor).
Power Consumption	24V, 600W.
Tether	50m in testing pool configuration.
Thrusters	6-Seabotix BTD150 continuous thrust 2.2kgf each with Syren 10 drivers.

2.2. Vehicle modelling

The kinematics and dynamics of low-inertia underwater vehicles, such as Leonard, rely on a mathematical representation involving 3D reference frames. These frames are the Earth-fixed frame which is usually placed at the water surface and the body-fixed frame, generally aligned with the vehicle's center of volume. Fig. 3 illustrates the arrangement of these frames, providing a clear visual representation of how they are assigned for the vehicle navigation based on SNAME (Society of Naval Architects and Marine Engineers) standard [23].

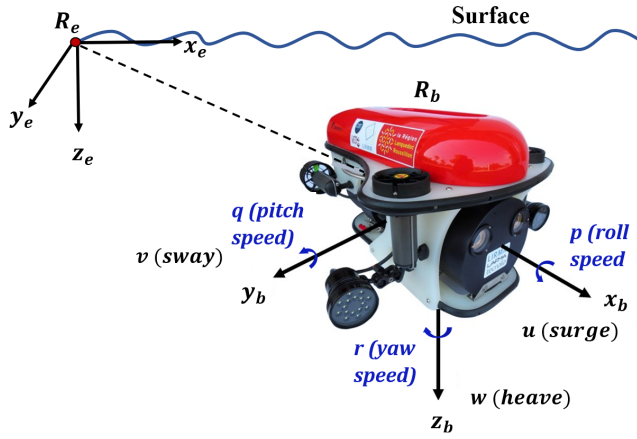


Figure 3: Illustration of the reference frames used in the vehicle modelling. The Earth-fixed frame is denoted (O_e, x_e, y_e, z_e) and the body-fixed frame is denoted (O_b, x_b, y_b, z_b) .

A. Kinematics

From the reference frames R_e and R_b , as illustrated in Fig. 3, we can relate the rate of change of the vehicle's position and orientation to its linear and angular velocities as follows:

$$\dot{\eta} = J(\eta)v \quad (1)$$

where $\eta = [\eta_1^T \ \eta_2^T]^T \in \mathbb{R}^{6 \times 1}$, with $\eta_1 = [x \ y \ z]^T$ and $\eta_2 = [\phi \ \theta \ \psi]^T$, is the vector of position and orientation in the Earth-fixed frame, $v = [v_1^T \ v_2^T]^T \in \mathbb{R}^{6 \times 1}$, with $v_1 = [u \ v \ w]^T$ and $v_2 = [p \ q \ r]^T$, is the linear and angular velocities vector in the body-fixed frame and $J(\eta) \in \mathbb{R}^{6 \times 6}$ is the 3D transformation matrix from R_e to R_b given by [23].

$$J(\eta) = \begin{bmatrix} J_1(\eta_2) & 0_{3 \times 3} \\ 0_{3 \times 3} & J_2(\eta_2) \end{bmatrix} \quad (2)$$

where $J_1(\eta_2)$ and $J_2(\eta_2)$ are given by:

$$J_1(\eta_2) = \begin{bmatrix} c\psi c\theta & c\psi s\theta s\phi - s\psi c\phi & c\psi s\theta c\phi + s\psi s\phi \\ s\psi c\theta & s\psi s\theta s\phi + c\psi c\phi & s\psi s\theta c\phi - c\psi s\phi \\ -s\theta & c\theta s\phi & c\theta c\phi \end{bmatrix} \quad (3)$$

$$J_2(\eta_2) = \begin{bmatrix} 1 & s\phi t\theta & c\phi t\theta \\ 0 & c\phi & -s\phi \\ 0 & s\phi/c\theta & c\phi/c\theta \end{bmatrix} \quad (4)$$

With $c(\cdot) \equiv \cos(\cdot)$, $s(\cdot) \equiv \sin(\cdot)$ and $t(\cdot) \equiv \tan(\cdot)$.

B. Dynamics

Following the SNAME convention and the representation proposed in [23], the dynamics of underwater vehicles in the body-fixed frame, can be expressed as follows:

$$M\dot{v} + C(v)v + D(v)v + g(\eta) = \tau + w(t) \quad (5)$$

where $M \in \mathbb{R}^{6 \times 6}$ is the inertia matrix including the effects of both rigid-body and added mass, $C(v) \in \mathbb{R}^{6 \times 6}$ is the Coriolis–centripetal matrix, $D(v) \in \mathbb{R}^{6 \times 6}$ is the hydrodynamic damping matrix, $g(\eta) \in \mathbb{R}^{6 \times 1}$ is the vector of restoring forces and moments, $\tau \in \mathbb{R}^{6 \times 1}$ is the control inputs vector, and $w(t) \in \mathbb{R}^{6 \times 1}$ is a time-varying vector representing the external disturbances.

Based on the dynamics equation (5), the matrices and vectors describing the dynamics are given as follows: The so-called inertia matrix M combining the vehicle's rigid-body inertia M_{RB} and the inertia of the added mass M_A can be expressed as follows:

$$M = M_{RB} + M_A \quad (6)$$

Besides, considering that the vehicle is moving at low speeds, the matrix M can be simplified as follows:

$$M = \text{diag}(m + X_u, m + Y_v, m + Z_w, I_{xx} + K_p, I_{yy} + M_q, I_{zz} + N_r) \quad (7)$$

where m is the mass of the vehicle, $\{I_{xx}, I_{yy}, I_{zz}\}$ are the vehicle's rigid-body moments of inertia and $\{X_u, Y_v, Z_w, K_p, M_q, N_r\}$ are the hydrodynamics added masses. Similarly, the damping matrix $D(v)$ can be approximated in R_b as follows:

$$D(v) = \text{diag}(X_u, Y_v, Z_w, K_p, M_q, N_r) \quad (8)$$

Moreover, the vector of restoring forces and moments $g(\eta)$ can be expressed as follows:

$$g(\eta) = \begin{bmatrix} -fs\theta \\ fc\theta s\phi \\ fc\theta c\phi \\ z_G W c\theta s\phi \\ z_G W s\theta \\ 0 \end{bmatrix} \quad (9)$$

where $f = W - B$, with W and B representing the weight and buoyancy of the *Leonard UUV* and $(0, 0, z_G)$ is the position of the vehicle's center of gravity. Finally, τ refers to the vector of control inputs responsible for translational and rotational motions of the vehicle. Thus, τ can be written as follows:

$$\tau = T.f \quad (10)$$

where $T \in \mathbb{R}^{6 \times 6}$ is the thrusters configuration matrix and $f = [f_1 \ f_2 \ f_3 \ f_4 \ f_5 \ f_6]^T$ is a vector of the forces produced by the six thrusters of the vehicle.

3. Proposed control scheme's design

This section outlines the design of the advanced RISE feedback control based on a fuzzy inference system, a novel contribution of this study. The conventional RISE feedback control approach, despite its proven effectiveness in various

applications [20], faces some specific challenges when implemented in real-time systems, particularly those restricted by cost or hardware. These challenges include a lack of adaptability due to its fixed gains, complexity in handling nonlinearities, potential difficulties when confronted with unexpected system uncertainties and risks of actuators saturation due to uncontrolled integral term growth [19].

To deal with these challenges, we propose a fusion of the RISE feedback control scheme with a fuzzy logic inference system. By incorporating fuzzy logic, the gain can be dynamically adjusted in real-time, enhancing adaptability and performance consistency. The inherent capability of fuzzy logic to work with linguistic variables provides an effective counter to system nonlinearities [24]. Its integration with RISE also adds a layer of robustness, enhancing resilience against unexpected disturbances, and allows for monitoring and automatically adjusting the gain to mitigate issues associated with integral wind-up. Furthermore, the fuzzy logic controller reduces the reliance on exact mathematical models, making them particularly advantageous when dealing with highly complex or ambiguous system dynamics [25].

Guided by these principles, the proposed solution not only retains the robustness of the traditional RISE control but also leverages the intuitive intelligence of fuzzy logic to offer smooth, auto-tuned control. The detailed design is detailed in the sequel, starting with a background on RISE feedback control followed by the enhanced controller design based on a fuzzy inference system.

3.1. Background on RISE feedback control

The RISE (Robust Integral of the Sign of the Error) feedback control is a robust nonlinear control strategy, developed for high-order nonlinear MIMO systems. This control scheme uses a non-model-based state feedback law to ensure semi-global asymptotic tracking. The RISE control uses a unique integral of sign of the error as a robustness term, in addition to the proportional integral part, to compensate for a wide range of uncertainties and external disturbances [18]. This makes the RISE control robust, while generating continuous control signals, avoiding chattering effects, and improving the tracking performance.

Let us first consider $\eta_d(t)$ as the desired trajectory for the vehicle, and $\eta(t)$ as its actual trajectory.

$$\eta_d(t) = [x_d(t), y_d(t), z_d(t), \phi_d(t), \theta_d(t), \psi_d(t)]^T \quad (11)$$

$$\eta(t) = [x(t), y(t), z(t), \phi(t), \theta(t), \psi(t)]^T \quad (12)$$

The vehicle tracking error $e_1(t)$ and its first time-derivative are defined as follows:

$$e_1(t) = \eta_d(t) - \eta(t) \quad (13)$$

$$\dot{e}_1(t) = \dot{\eta}_d(t) - \dot{\eta}(t) \quad (14)$$

Where $\dot{\eta}_d(t)$ and $\dot{\eta}(t)$ are the first time-derivatives of $\eta_d(t)$ and $\eta(t)$, respectively, $e_1(t) = [e_{1x}(t), e_{1y}(t), \dots, e_{1\psi}(t)]^T$ and $\dot{e}_1(t) = [\dot{e}_{1x}(t), \dot{e}_{1y}(t), \dots, \dot{e}_{1\psi}(t)]^T$. An auxiliary tracking error is introduced as follows:

$$e_2(t) = \dot{e}_1(t) + \alpha_1 e_1(t) \quad (15)$$

where $\alpha_1 > 0$ is a positive constant.

Based on the stability analysis established in [18], the RISE control law can be formulated for the vehicle's six degrees of freedom as follows:

$$\begin{aligned} \tau = & (k_s + I)e_2(t) - (k_s + I)e_2(t_0) \\ & + \int_0^t (k_s + I)\alpha_2 e_2(\sigma) d\sigma \\ & + \int_0^t \beta \text{sgn}(e_2(\sigma)) d\sigma \end{aligned} \quad (16)$$

Where $\tau \in \mathbb{R}^{6 \times 6}$ is the control input vector, $I \in \mathbb{R}^{6 \times 6}$ is the identity matrix and $\text{sgn}(\cdot)$ represents the standard signum function. Additionally, k_s , α_2 and $\beta \in \mathbb{R}^{6 \times 6}$ are positive definite diagonal feedback gain matrices expressed as:

$$k_s = \begin{bmatrix} k_{s1} & 0 & \dots & 0 \\ 0 & k_{s2} & \dots & 0 \\ \vdots & \vdots & \ddots & \vdots \\ 0 & 0 & \dots & k_{s6} \end{bmatrix} \quad \beta = \begin{bmatrix} \beta_1 & 0 & \dots & 0 \\ 0 & \beta_2 & \dots & 0 \\ \vdots & \vdots & \ddots & \vdots \\ 0 & 0 & \dots & \beta_6 \end{bmatrix}$$

$$\alpha_2 = \begin{bmatrix} \alpha_{21} & 0 & \dots & 0 \\ 0 & \alpha_{22} & \dots & 0 \\ \vdots & \vdots & \ddots & \vdots \\ 0 & 0 & \dots & \alpha_{26} \end{bmatrix}$$

It is worth noting that the second term of equation (16), i.e., $(k_s + I)e_2(t_0)$ is introduced to ensure a zero-control input at initial time $t = t_0$ (that is, $u(t_0) = 0$).

3.2. Proposed control scheme: A fuzzy-based RISE control

To achieve effective control with the RISE command, its parameters must be carefully tuned and set to their optimal values. The feedback gain k_s is often regarded as having the most significant influence on the RISE control performance since it dictates the rate at which the controller reacts to regulation errors. This rate can impact both system's stability and accuracy. Too high values of k_s may lead to oscillations and instability, while too low values can result in a slow response and a limited precision [26]. Given these challenges, there is a compelling need for a method that can automatically adjust the k_s gain while considering the dynamic conditions and ensuring optimal performance. Fuzzy logic emerges as a promising solution to address this necessity by adjusting the k_s feedback gain based on various system states and behaviors.

Fuzzy logic is a human-like intelligent inference method that embodies human control experience and strategy. Unlike traditional methods relying on precise models of nonlinear control systems, fuzzy control can be applied in the control process, offering strong robustness and excellent anti-interference performance [27]. Fuzzy control, with its innate adaptability and decision-making capabilities, is effective in settings where precise mathematical models are either lacking or overly complex.

In this study, a Mamdani-type fuzzy controller is proposed with two-inputs : the robot's tracking error e_1 and its first time-derivative \dot{e}_1 , and a single output : the adaptive feedback gain k_s . This controller integrates three core components: fuzzification, fuzzy inference system, and defuzzification [28].

A. Fuzzification

For the fuzzification step, the system employs a carefully selected set of Gaussian membership functions to convert numerical inputs into fuzzy values. These functions are chosen based on two primary considerations, including (i) their ability to ensure a smooth and continuous transition, thus reducing sudden changes, and (ii) the simplicity of their mathematical representation which helps in computation.

This conversion process is essential for the application of fuzzy logic rules within the inference engine. By converting crisp values, the system's input parameters such as the robot's tracking error e_1 and its first time-derivative \dot{e}_1 , into fuzzy sets, the system can interpret and process these inputs in terms of linguistic variables like Large Negative, Negative, Zero, Positive, and Large Positive. This interpretation aligns with the human-like reasoning approach that fuzzy logic aims to emulate, where decisions are made based on degrees of truth rather than binary logic.

To achieve this transformation, five Gaussian membership functions are employed, they are illustrated in Fig. 4. These functions, denoted as μ_{e_1} for the tracking error and $\mu_{\dot{e}_1}$ for its first time-derivative, indicate the degree of membership of each variable to the fuzzy sets.

To precisely define the Gaussian functions, a_1 and a_2 are set as the centers for μ_{e_1} curves, determining the peak points of membership for the tracking error, while b_1 and b_2 are the centers for $\mu_{\dot{e}_1}$ curves, governing the peak points for the first time-derivative of the tracking error. These central points are critical as they reflect where the input values have the highest degree of membership to the corresponding fuzzy sets, thereby dictating the system's response to changes in tracking error and its first time-derivative.

B. Fuzzy inference system

The core of the fuzzy logic system is the fuzzy rule base, a collection of *if-then* rules that define how the inputs are mapped to the output. The rules are formulated based on expert knowledge and intuition about the control system's behavior, ensuring that the system's responses are both precise and adaptable to changing conditions. For instance, if the tracking error is 'Positive Large' (PL) and the error

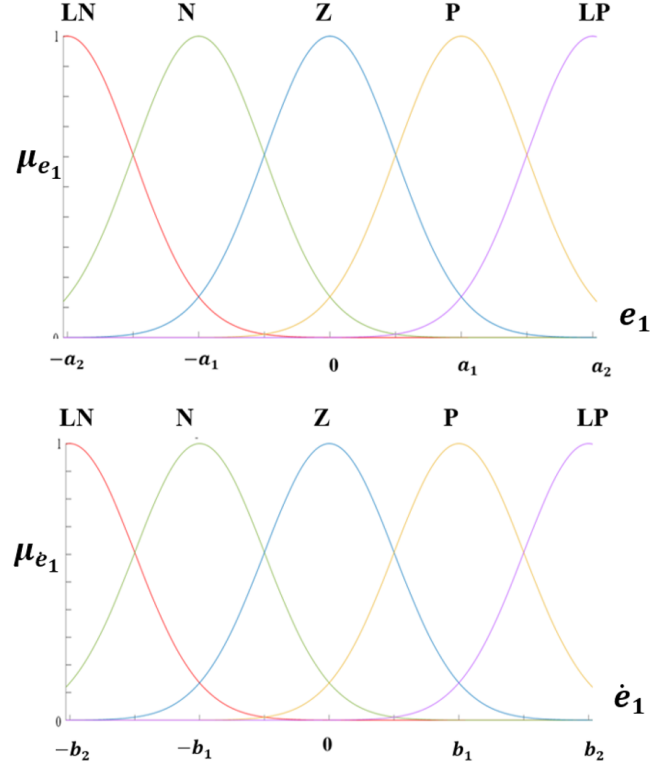


Figure 4: Membership functions for input variables.

change rate is 'Positive Small' (PS), then the feedback gain might be finely adjusted to a 'Medium' (M) value, to correct the trajectory efficiently without causing overshoots or instability. The rule base effectively captures the relationship between the tracking performance and the necessary adjustments to the feedback gain, providing a mechanism for a dynamic adaptation.

By adopting a trial-and-error approach to assess various fuzzy control rules, a definitive set of rules for UUV path tracking was formulated. This set results from thorough testing and fine-tuning, leveraging the inherent strengths of fuzzy logic designed to mimic human decision-making. Such a manual selection process is suitably tuned through observed performance and expert intuition, enabling the system to automatically compute and adjust the output parameter, i.e., the gain k_s , based on the values of e_1 and \dot{e}_1 . This dynamic adjustment mechanism, summarized in Table 2, clearly demonstrates the system's ability to adapt to real-time changes in the vehicle's tracking error and its rate of change, enhancing both effectiveness and reactivity.

C. Defuzzification

For the defuzzification phase, the fuzzy output generated by the inference engine is transformed back into a crisp control signal, facilitating practical implementation in the control system.

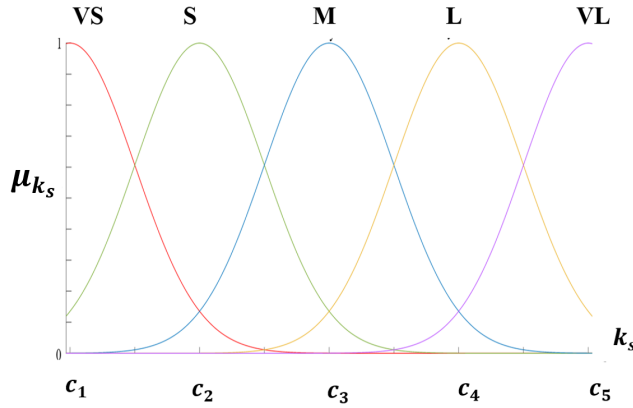
The center of gravity method, renowned for producing smooth outputs that responsively adapt to even minor input changes, is selected as the defuzzification strategy for this

Table 2

Table of the fuzzy rules base.

$e_1 \backslash \dot{e}_1$	Large Negative	Negative	Zero	Positive	Large Positive
Large Negative	Very small	Very small	Very small	Small	Medium
Negative	Very small	Very small	Small	Medium	Large
Zero	Very small	Small	Medium	Large	Very large
Positive	Small	Medium	Large	Very large	Very large
Large Positive	Medium	Large	Very large	Very large	Very large

investigation. This method determines the crisp value by pinpointing the center of mass along the output membership function curve. This is achieved by identifying the point where the cumulative distribution of fuzzy output values is equally balanced on both sides. Fig. 5 illustrates the membership functions for the output variable, specifically the gain k_s . The membership function μ_{k_s} is parameterized by the constants c_1 through c_5 , which correspond to the centers of the Gaussian curves for the linguistic terms Very Small (VS), Small (S), Medium (M), Large (L), and Very Large (VL), respectively. These centers define the points of highest membership for each term and are critical for accurately interpreting the output's degree of membership in the respective fuzzy sets.


Figure 5: Membership functions for output variable.

The conversion of fuzzy results into a single numerical output is meticulously handled by the COG (Center of Gravity) method, with the defuzzified output calculated accordingly:

$$k_{s_{\text{fuzzy}}} = \frac{c_1\mu_{\text{VS}} + c_2\mu_{\text{S}} + c_3\mu_{\text{M}} + c_4\mu_{\text{L}} + c_5\mu_{\text{VL}}}{\mu_{\text{VS}} + \mu_{\text{S}} + \mu_{\text{M}} + \mu_{\text{L}} + \mu_{\text{VL}}} \quad (17)$$

Where VS: Very Small, S: Small, M: Medium, L: Large, VL: Very Large.

And:

$$\begin{cases} \mu_{\text{VS}} = \max(\mu_{R1}, \mu_{R2}, \mu_{R3}, \mu_{R6}, \mu_{R7}, \mu_{R11}) \\ \mu_{\text{S}} = \max(\mu_{R4}, \mu_{R8}, \mu_{R12}, \mu_{R16}) \\ \mu_{\text{M}} = \max(\mu_{R5}, \mu_{R9}, \mu_{R13}, \mu_{R17}, \mu_{R21}) \\ \mu_{\text{L}} = \max(\mu_{R10}, \mu_{R14}, \mu_{R18}, \mu_{R22}) \\ \mu_{\text{VL}} = \max(\mu_{R15}, \mu_{R19}, \mu_{R20}, \mu_{R23}, \mu_{R24}, \mu_{R25}) \end{cases} \quad (18)$$

With:

$$\begin{cases} \mu_{R1} = \min(\mu_{\text{LN}}(e_1), \mu_{\text{LN}}(\dot{e}_1)) \\ \mu_{R2} = \min(\mu_{\text{N}}(e_1), \mu_{\text{N}}(\dot{e}_1)) \\ \vdots \\ \mu_{R25} = \min(\mu_{\text{LP}}(e_1), \mu_{\text{LP}}(\dot{e}_1)) \end{cases} \quad (19)$$

The constants $a_1, a_2, b_1, b_2, c_1, c_2, c_3, c_4,$ and c_5 are tuned using the trial-and-error technique.

The use of the trial-and-error technique for tuning the fuzzy inference system is particularly effective because it aligns with the foundational principles of fuzzy logic. Fuzzy logic is inherently based on reproducing human expertise and observational learning. Therefore, the trial-and-error method is a strategic choice that exploits the human-like decision-making process innate to fuzzy systems. This approach efficiently captures and translates expert insights into the control logic.

Ultimately, the resulting control law can be expressed by:

$$\begin{aligned} \tau_{\text{RISE}} = & (k_s(\cdot) + I)e_2(t) - (k_s(\cdot) + I)e_2(t_0) \\ & + \int_0^t (k_s(\cdot) + I)\alpha_2 e_2(\sigma) d\sigma \\ & + \int_0^t \beta \text{sgn}(e_2(\sigma)) d\sigma \end{aligned} \quad (20)$$

Where $k_s(\cdot)$ is the output of the fuzzy inference system and FRISE refers to the enhanced RISE controller using fuzzy logic.

4. Real-time experimental results

In this section, we present the obtained real-time experimental results including various scenarios using the Leonard underwater vehicle described in Section 2.1. During the real-time validation, different scenarios were considered to assess the effectiveness of the proposed enhanced RISE controller in comparison to the conventional RISE controller. It was also evaluated in terms of robustness against uncertainties and external disturbances. Additionally, the PID controller was also implemented and serves as a benchmark for comparison.

4.1. Some real-time implementation issues

Even though the previous section addressed the theoretical design of the proposed RISE and FRISE controllers for

all the six DOFs, the real-time validations of the proposed control schemes will focus only on the autonomous control of two DOFs for performance evaluation. The two DOFs in question include one translational DOF (depth) and one rotational DOF (yaw), for the following technical reasons: (i) The measurement of the depth (z) is affected by noise, primarily attributed to the used pressure sensor. (ii) Practical marine operations often demand precise control of the vehicle's yaw. For instance, activities like oceanography and dam inspection [29] heavily rely on accurate yaw control. (iii) In contrast, the surge (x) and sway (y) DOFs of the vehicle are both difficult to measure. Besides, the roll (ϕ) and pitch (θ) DOFs exhibit passive stability characteristics thanks to the design of our vehicle.

During the testing phase, the vehicle is controlled to track the desired depth and yaw trajectories as accurately as possible in different operating conditions. They include, internal/external disturbances, parametric uncertainties, unmodelled dynamics and unpredictable operating environments.

All the conducted tests in this study were carried out in the 4x3x2 m testing pool at LIRMM laboratory for various scenarios, as illustrated in Fig 6.

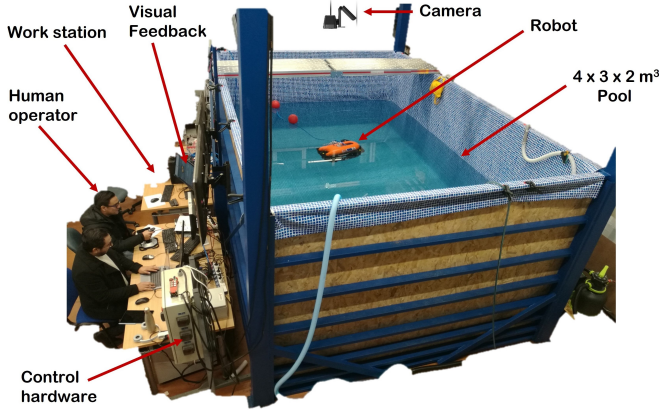


Figure 6: Illustration of the experimental environment.

4.2. Proposed experimental scenarios

In order to evaluate the efficiency and robustness of the proposed control scheme, we propose the following **four** main scenarios:

(1) Scenario 1: Nominal case

In this scenario, the robot is guided along a predefined reference trajectory in depth and yaw (illustrated in Fig 7) in the absence of external disturbances and parametric uncertainties. During this test, the controller's gains are tuned to ensure the best tracking and are kept unchanged for the other scenarios.

(2) Scenario 2: Robustness towards parametric uncertainties

In this test, the vehicle's buoyancy and damping are modified to evaluate the robustness of the proposed approach towards parametric uncertainties (Fig 8).

(3) Scenario 3: External disturbances rejection

In this scenario, the Leonard vehicle is evaluated for its robustness against various external disturbances in marine settings, such as sudden collisions, tool manipulations and strong water currents. These situations are emulated with a strong push applied to the vehicle's body using a long stick as shown in Fig 9. The aim of this scenario is to evaluate the effectiveness of each controller to keep the vehicle close to the desired trajectories.

(4) Scenario 4: Combined parametric uncertainties and external disturbances

In this scenario, the vehicle is subject to a combination of parametric uncertainties and external disturbances to evaluate the robustness of the proposed control scheme in a further challenging scenario. The vehicle's buoyancy and damping parameters are modified as in Scenario 2, while the vehicle is exposed to external disturbances, as described in Scenario 3.

4.3. Tracking performance indices

To numerically quantify the tracking performance of the proposed control scheme, a performance index known as the Root Mean Square Error (RMSE) is utilized, it is defined as follows:

$$\text{RMS}(e_1(t))_{\text{position/orientation}} = \sqrt{\frac{1}{T_f} \int_0^{T_f} \|e_1(t)\|^2 dt} \quad (21)$$

where $e_1(t)$ represents the tracking error, and T_f is the test duration.

Additionally, energy consumption is evaluated by computing the integral of control input efforts (force and torque) as follows:

$$\text{INT}(\tau) = \int_0^{T_f} \|\tau(t)\| dt \quad (22)$$

where τ represents the vector of control inputs.

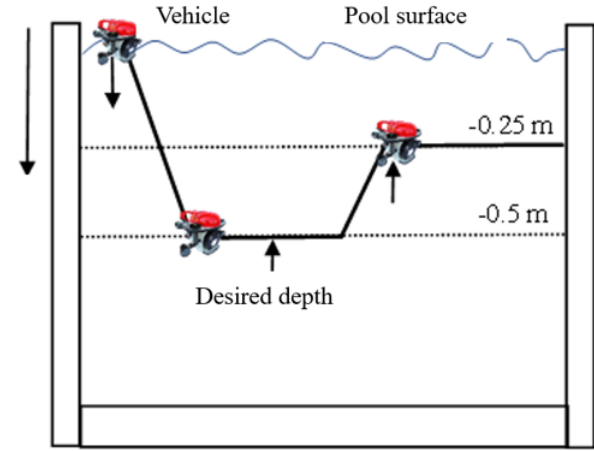
In the subsequent sections, the RMSE for yaw and depth are denoted RMSE_ψ and RMSE_z , respectively. The terms INT_ψ and INT_z represent the integral of control input for yaw and depth, respectively.

4.4. Tuning of the feedback control gains

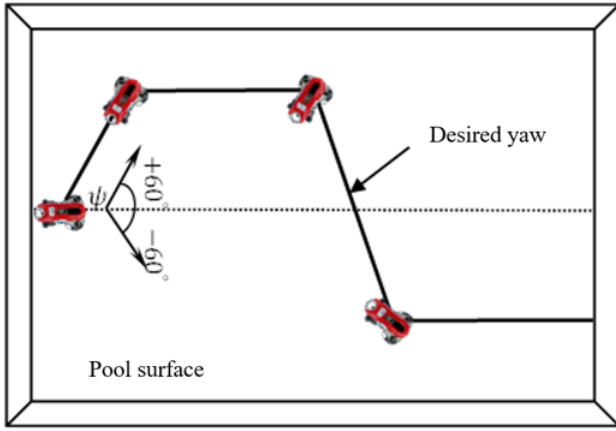
The tuning process for the standard RISE control gains is experimentally conducted according to the following algorithm:

Algorithm 1 : Feedback Control Parameters Tuning

- (1) Initially, set $\alpha_2 = 0$ and $\beta = 0$.



(a)



(b)

Figure 7: Illustration of the predefined desired trajectories, (a) desired depth and (b) desired yaw.

- (2) Tune α_1 and k_s as if it were a PD controller, with $\alpha_1(k_s + 1)$ as the proportional gain and $(k_s + 1)$ as the derivative gain until achieving satisfactory tracking.
- (3) Gradually increase α_2 while adjusting α_1 and k_s , either increasing or decreasing, to optimize performance.
- (4) Increase β until the input signal exhibits less chattering and improved performance.

The resulting RISE control parameters used during the real-time experiments are summarized in Table 5.

4.5. Obtained real-time experimental results

A. Scenario 1: Nominal case

In this scenario, the vehicle is controlled to follow predefined trajectories on both depth and yaw, despite internal disturbances such as measurement noise. External disturbances and parametric uncertainties are first excluded to obtain the best feedback gains for use in subsequent scenarios. Initially, the robot submerges to a depth of 50 cm from the water's

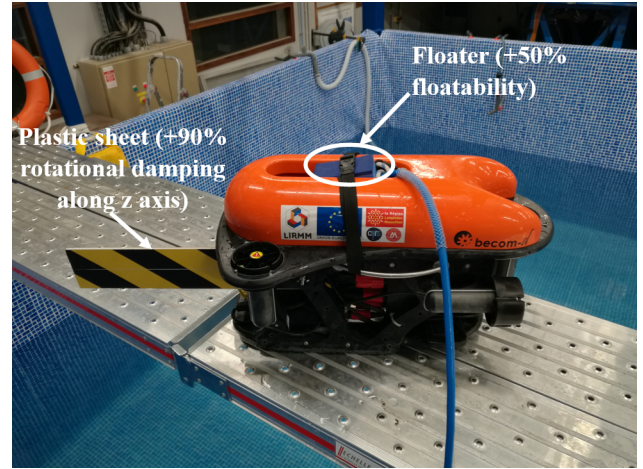


Figure 8: Illustration of a reconfiguration of the vehicle to introduce parametric uncertainties: (the floater changes the vehicle's floatability by +50%, while the rigid plastic sheet increases the rotational drag on the yaw by +90%).

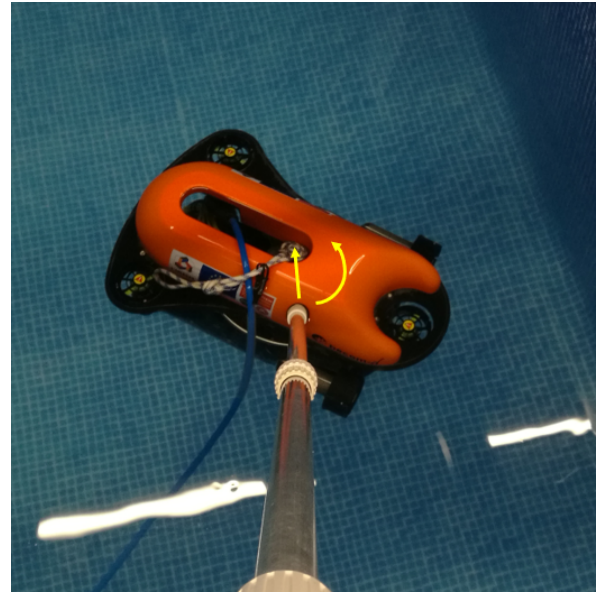


Figure 9: Illustration of the applied external disturbances.

surface and stays at this depth for 20 seconds. It then ascends to 25 cm, maintaining this position until the test concludes. Concurrently, the robot rotates in yaw from its starting position to $+60^\circ$ within 6 seconds and sustains that orientation for the next 20 seconds. Subsequently, it rotates back to -60° and holds this position for the remainder of the trial. This test aims to adjust the feedback gains of each control solution in real time for a fair comparison. The gains that ensure the best performance are retained for the subsequent scenarios. It is worth noting that the parameters α_1 , α_2 , and β for the RISE and FRISE controllers are identical, except for the feedback gain k_s , which remains for constant for the standard RISE controller and is adapted online for the proposed FRISE controller. Additionally, the centers of the membership functions for the FRISE controller are denoted

Table 3

Root mean square error (RMSE) and improvement for the three controllers.

Case	RMSE _z [m]			Improvement	
	PID	RISE	FRISE	Imp _{/PID}	Imp _{/RISE}
S1	0.02275	0.01193	0.01077	52.66%	9.72%
S2	0.04480	0.01553	0.01315	70.65%	15.33%
S3	0.03762	0.03594	0.02134	43.27%	40.62%
S4	—	—	0.02810	—	—
Case	RMSE _ψ [deg]			Improvement	
	PID	RISE	FRISE	Imp _{/PID}	Imp _{/RISE}
S1	2.46179	1.64854	1.64303	33.26%	0.33%
S2	2.10279	1.86353	1.70606	18.87%	8.45%
S3	3.35944	2.44440	1.96593	41.48%	19.57%
S4	—	—	2.63917	—	—

Table 4

Energy consumption comparison criteria through the INT indicator for the three controllers.

INT	Case	PID	RISE	FRISE
INT _z	S1	149790.307	162878.784	167944.57
	S2	297976.241	259551.913	310037.91
	S3	186415.499	215950.352	209658.54
	S4	—	—	274139.36
INT _ψ	S1	16442.961	20523.509	21951.78
	S2	13184.905	17807.280	19489.25
	S3	23174.006	25145.814	22175.55
	S4	—	—	34853.46

Table 5

Control parameters used in the conducted experiments.

	PID	RISE	FRISE
Depth	$k_{p,z} = 40$	$k_{s,z} = 5$	$c_{1,z} = 3$
	$k_{i,z} = 1$	$\beta_z = 0.01$	$c_{2,z} = 4$
	$k_{d,z} = 2$	$\alpha_{1,z} = 10$	$c_{3,z} = 5$
		$\alpha_{2,z} = 0.5$	$c_{4,z} = 7$
			$c_{5,z} = 10$
Yaw	$k_{p,\psi} = 8$	$k_{s,\psi} = 1.1$	$c_{1,\psi} = 0.7$
	$k_{i,\psi} = 0.1$	$\beta_\psi = 0.01$	$c_{2,\psi} = 0.9$
	$k_{d,\psi} = 4$	$\alpha_{1,\psi} = 5$	$c_{3,\psi} = 1.2$
		$\alpha_{2,\psi} = 0.5$	$c_{4,\psi} = 1.4$
			$c_{5,\psi} = 1.6$

by (c_1 to c_5). The resulting parameters of the implemented controllers are summarized in Table 5, where the index 'z' refers to the depth and the 'ψ' index refers to the yaw. The obtained results for this scenario are depicted in Fig 10.

From Fig. 10 (top-left graph), it is evident that all the three controllers effectively guide the vehicle to follow the desired depth trajectory. However, the depth tracking error of the PID controller is slightly higher than those of the other two controllers, as illustrated by the middle-left graph. In terms of yaw tracking, all controllers demonstrate their capability to accurately track the desired yaw, as it can be observed on the top-right graph. Yet, the yaw tracking error

for the PID controller is marginally larger, as depicted in the middle-right graph. In this context, the proposed FRISE (fuzzy-RISE) scheme appears to behave similarly to the RISE controller. Both controllers converge to the reference trajectory in a short span of time, exhibiting a minor tracking error as observed in the error plot in the middle plots of Fig. 10. This observation aligns with the numerical data from the root mean square error (RMSE) presented in Table 3. Notably, Table 3 underscores the superior performance of the proposed FRISE design over the conventional RISE approach, enhancing the tracking performance for the depth trajectory by approximately 52.66% compared to the PID controller, and by 9.72% with respect to the RISE controller. Similarly, for the yaw tracking performance, FRISE offers respectively an improvement of 33.26% over PID and 0.33% over RISE controllers.

Finally, the evolution of the control inputs is displayed at the bottom plots of Fig. 10. The computed values of the integral are summarized in Table 4. To compare the energy consumption for trajectory tracking of depth and yaw dynamics for both RISE and FRISE controllers, we need to divide INT_z and INT_ψ for each methodology as follows:

$$\frac{\text{INT}_{z\text{FRISE}}}{\text{INT}_{z\text{RISE}}} = \frac{167944.57}{162878.78} = 1.03;$$

$$\frac{\text{INT}_{\psi\text{FRISE}}}{\text{INT}_{\psi\text{RISE}}} = \frac{21951.78}{20523.40} = 1.06$$

This means that energy consumption for trajectory tracking in depth, using the FRISE controller, is 1.03 times the energy consumption using the RISE control. Energy consumption for trajectory tracking in yaw using the FRISE controller is 1.06 times the energy consumption using the RISE controller in the nominal scenario. In summary, alongside the FRISE controller's superior tracking performance, its energy consumption is approximately equivalent to that of the RISE controller for both depth and yaw tracking. This shows that the FRISE controller slightly outperforms the RISE controller and clearly outperforms the PID controller in terms of tracking accuracy in the nominal scenario.

B. Scenario 2: Robustness towards parametric uncertainties

The objective of this scenario is to evaluate the robustness of each controller against parametric variations, such as changes in the vehicle's floatability and damping. To elaborate this change, we attached a rigid plastic sheet measuring 0.45 m × 0.1 m to the side of the vehicle. This leads to an increase in the damping term $D(\cdot)$ by $\Delta D(\cdot) = +90\%$ of its nominal value. In a similar manner, the floatability term $B - W$ is increased by +50% of its nominal value by attaching a float to the top of the vehicle, as illustrated in Fig. 8. The modified vehicle is controlled to follow the same reference trajectories as designed in Fig. 7 (similar to the nominal scenario).

The AUV trajectory tracking for depth and yaw motions in this scenario are displayed at the top plots of Fig. 11.

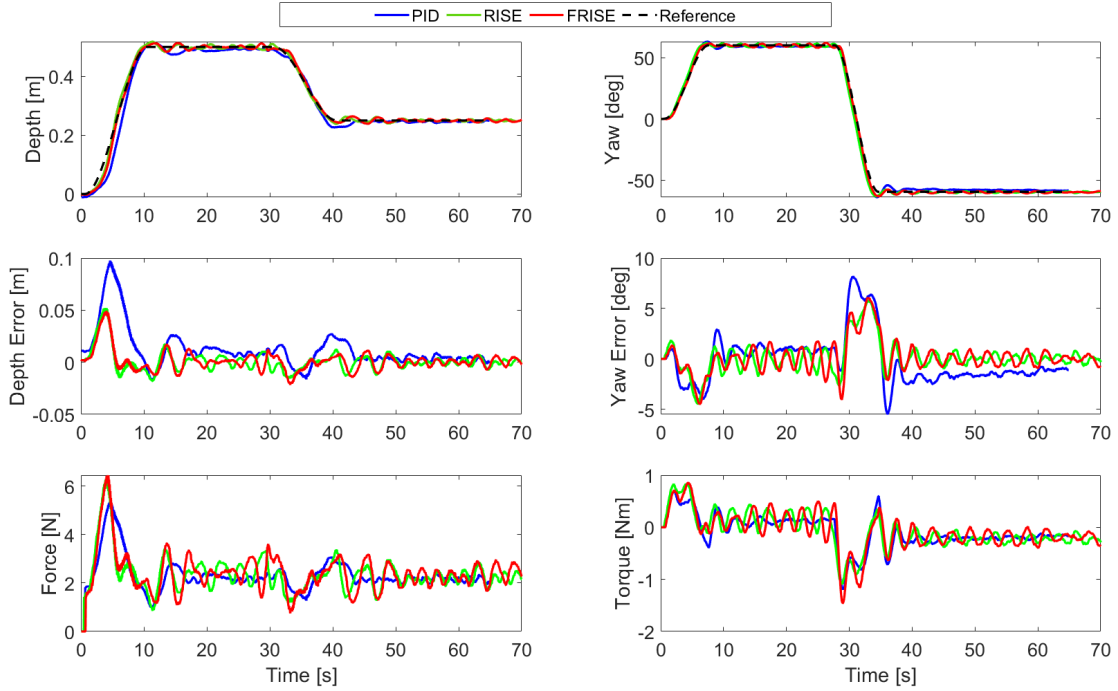


Figure 10: Real-time experimental results for the nominal case: (top graphs) tracking of depth and yaw, (middle graphs) corresponding tracking errors for depth and yaw, (bottom graphs) evolution versus time of the vehicle's control inputs.

From this figure, it can be observed that the introduced uncertainties clearly highlight the weakness of the PID control scheme, particularly in terms of depth tracking. As can be seen in the top-left plot, the robot is no longer able to compensate for the depth position error and operates 5 cm away from the desired trajectory. Consequently, the controlled output starts to oscillate as the controller attempts to counteract the effects of parametric uncertainties. This observation is also confirmed by the middle-left plot of Fig. 11.

Besides, this test indicates that the tracking precision for yaw and depth of the conventional RISE controller remains overall robust despite the presence parametric uncertainties in the vehicle dynamics. Furthermore, incorporating the fuzzy logic controller into this robust controller further enhances both depth and yaw tracking. The enhanced controller can precisely follow the reference trajectory even in the presence of parametric uncertainties. The tracking errors are depicted in the middle graphs of Fig. 11, and their numerical quantification is presented in Table 3. **The FRISE controller improves depth tracking by 70.65% over PID and 15.33% over RISE, and the yaw tracking by 18.87% and 8.45%, respectively.** The evolution of the input signals is displayed at the bottom plots of Fig. 11. Finally, based on the obtained results displayed in Table 4, the quotients between INT_z and INT_ψ from the robustness toward parametric uncertainties test are:

$$\frac{INT_{z_{FRISE}}}{INT_{z_{RISE}}} = \frac{310037.91}{295951.91} = 1.04$$

$$\frac{INT_{\psi_{FRISE}}}{INT_{\psi_{RISE}}} = \frac{19489.25}{17807.28} = 1.09$$

This means that the energy consumption for depth of the FRISE control is only 1.04 times higher than the consumption of the RISE. Moreover, the energy consumption for the heading tracking is also very similar for both schemes. Finally, this scenario illustrates the superiority of the FRISE controller compared to PID and RISE controllers in terms of rejecting parametric uncertainties.

C. Scenario 3: External disturbance rejection

In order to assess in more detail the effectiveness of the proposed control scheme against external disturbances during real-time operations, a series of successive external pushes was applied to the vehicle **by a human operator** using a long stick (cf. illustration of Fig. 9), affecting both the depth and yaw **dynamics** during the tracking task. However, it should be noted that **achieving a fair comparison is extremely challenging**, if not impossible, due to critical issues in experimental operating conditions. Specifically, the same magnitude and characteristics of external disturbances (time, application point, direction, etc) need to be uniformly applied across all real-time control schemes, a task practically unfeasible given the human-generated nature of these disturbances. Therefore, while it is difficult to make a strictly fair comparison based on these experiments, the tests still offer a qualitative overview of each control approach's behavior. The results obtained for each control scheme, presented in Figs. 12, 13 and 14, demonstrate their respective responses under similar but not perfectly identical conditions.

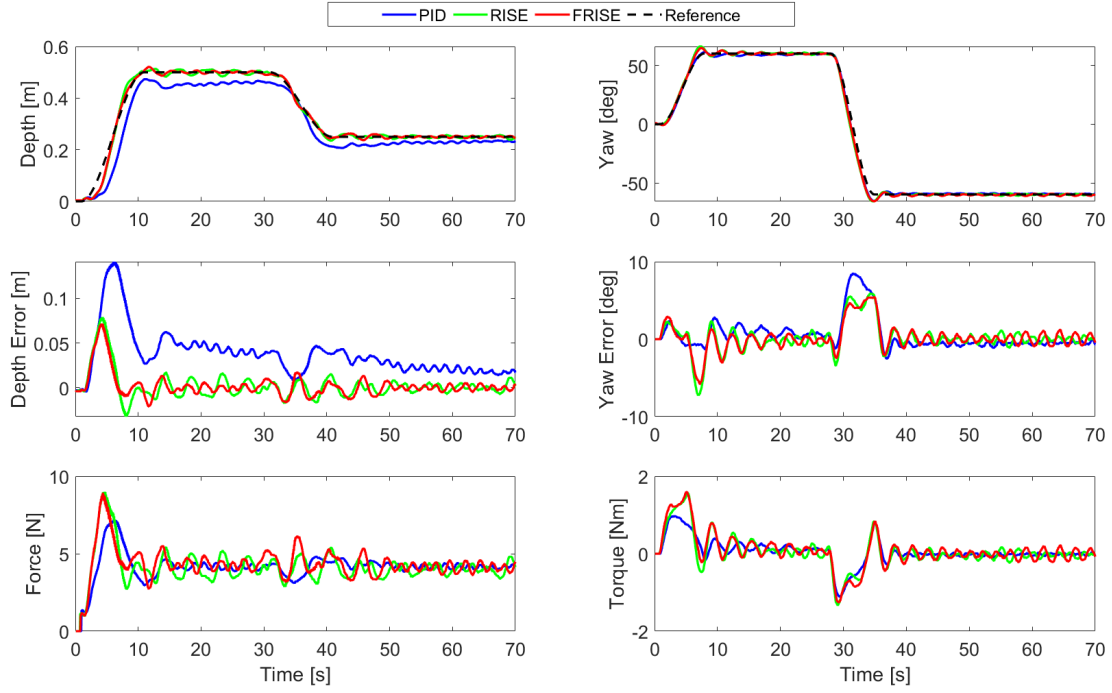


Figure 11: Robustness towards parametric uncertainties: (top graphs) tracking of depth and yaw, (middle graphs) corresponding tracking errors for depth and yaw, (bottom graphs) evolution versus time of the vehicle's control inputs.

Based on the graphs of these figures, we observe that the disturbances applied to the vehicle prevent the PID from converging to the desired depth until their influence is cancelled out. A static offset reappears in the depth tracking of this controller when the disturbance's effect becomes active again. In contrast, the other controllers neutralize the disturbance's influence and converge to the desired depth in a short span of time. However, RISE takes slightly longer time than its enhanced version FRISE to approach the desired depth due to the fixed feedback gains of the controller, as depicted in Fig. 13 and Fig. 14 (middle-left graph).

Concerning the yaw tracking, all controllers demonstrate good performance. The yaw trackings and their associated errors for all the controllers are presented in Fig. 12, 13 and 14 (top and middle-right graphs, respectively), whereas the numerical values of RMSE are given in Table 3. Moreover, the evolution of control input signals over time for depth and yaw during this mission are illustrated in the bottom graphs.

Finally, from the results displayed in Table 4, the quotients between INT_z and INT_ψ from the robustness toward external disturbances test are as follows:

$$\frac{INT_{z_{RISE}}}{INT_{z_{FRISE}}} = \frac{215950.35}{209658.54} = 1.03$$

$$\frac{INT_{\psi_{RISE}}}{INT_{\psi_{FRISE}}} = \frac{25145.81}{22175.55} = 1.13$$

This result means that the energy consumption for the trajectory tracking in depth is almost similar for both controllers. While the energy consumption for the tracking in heading for

the FRISE is 1.13 times higher than the energy consumption using the nominal RISE controller. Globally, one observes that the FRISE controller reduces the time needed to come back to the reference after a sudden disturbance, compared to the PID and the RISE controllers.

D. Scenario 4: Combined parametric uncertainties and external disturbances

In this scenario, the proposed FRISE controller is exclusively evaluated under combined parametric uncertainties and external disturbances, as described above in Section 4.2. The primary goal is to assess the controller's effectiveness and robustness within a challenging dynamic and uncertain environment that mirrors real-world marine conditions. During this test, the proposed FRISE controller is subject to simultaneous changes in buoyancy and damping parameters, along with unpredictable external disturbances. The obtained results are displayed in Fig. 15. The top plots of this figure clearly show the controller's rapid response, successfully recovering from four distinct disturbances in both depth and yaw dynamics. The associate tracking errors for both dynamics are plotted in the middle plots, demonstrating the controller's ability to maintain the vehicle around its desired trajectories. The bottom part of the figure displays the evolution of the input signals versus time, showing the controller's active response in neutralizing the applied disturbances. The RMSE metric values are summarized in Table 3, showing a minor increase when compared to the individual tests of parametric uncertainties and external disturbance. This attests that the proposed FRISE controller is able to handle

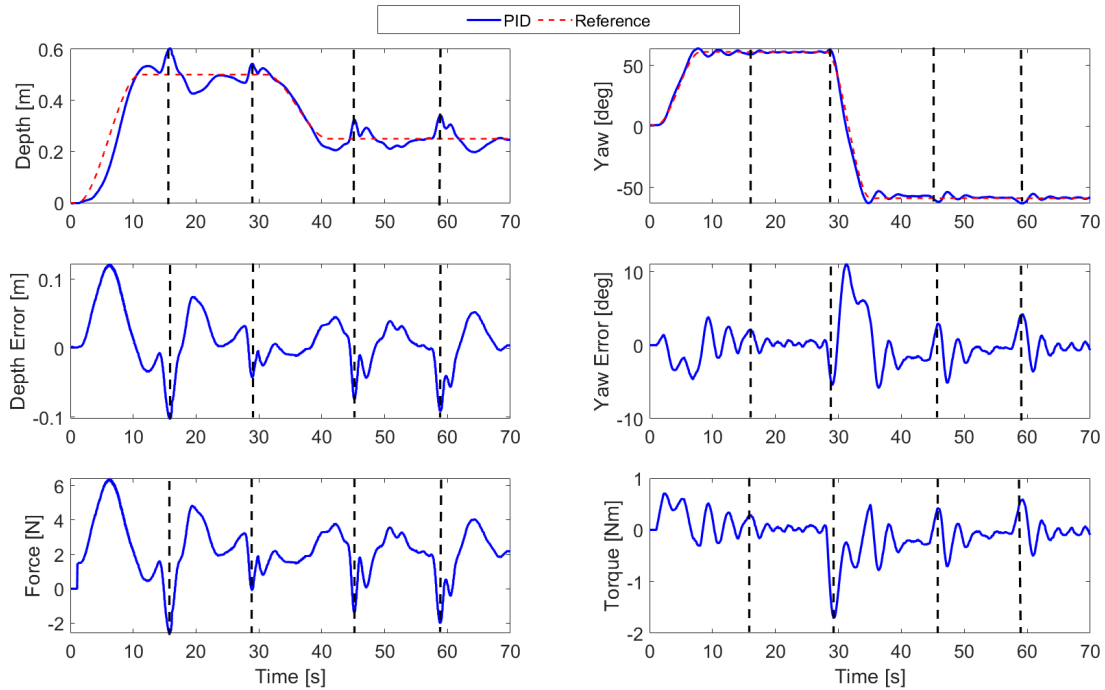


Figure 12: Robustness of the PID controller towards external disturbances: (top graphs) tracking of depth and yaw, (middle graphs) corresponding tracking errors for depth and yaw, (bottom graphs) evolution versus time of the vehicle's control inputs.

multiple challenges concurrently with minimal performance compromise. Furthermore, the evolution of the input signals versus time and their numerical quantification, displayed in Table 4, indicate clearly a marginal increase in energy consumption due to the compensated uncertainties and external disturbances. However, the increase remains within the admissible range since the actuators are far from their saturation limit. To sum up, the proposed FRISE controller demonstrates robust performance in this challenging scenario, validating its potential for practical applications in marine environments where both parametric uncertainties and external disturbances are prevalent.

5. Conclusion and future works

In this paper, we proposed an enhanced RISE controller for trajectory tracking of an AUV. The design of the nominal RISE controller is improved by incorporating a fuzzy logic inference system, which automatically tunes the parameters of the controller. This proposed controller has been implemented in real-time for trajectory tracking in both depth and yaw motions using the Leonard underwater vehicle. Furthermore, the proposed FRISE approach was studied and compared to both the standard RISE and the classical PID across various experimental scenarios. Real-time experimental results showcase the effectiveness, robustness, and enhancement of the proposed controller in dealing with uncertainties in system parameters, such as damping and buoyancy changes, as well as towards external disturbances. In future work, we may consider further optimizing the

fuzzy logic controller's rules and membership functions to improve the performances even more.

6. Acknowledgment

This work was supported by "Défi Clé Robotique centrée sur l'humain" (ROVAGUE project) funded by Région Occitanie, France.

References

- [1] Y. Yang, Y. Xiao and T. Li, "A Survey of Autonomous Underwater Vehicle Formation: Performance, Formation Control, and Communication Capability", *IEEE Communications Surveys and Tutorials*, vol. 23, no. 2, pp. 815-841, Secondquarter 2021, doi: 10.1109/COMST.2021.3059998.
- [2] J. Zhang, J. Sha, G. Han, J. Liu and Y. Qian, "A Cooperative-Control-Based Underwater Target Escorting Mechanism With Multiple Autonomous Underwater Vehicles for Underwater Internet of Things", *IEEE Internet of Things Journal*, vol. 8, no. 6, pp. 4403-4416, 15 March 2021, doi: 10.1109/IIOT.2020.3026355.
- [3] F. Kong, Y. Guo and W. Lyu, "Dynamics Modeling and Motion Control of a New Unmanned Underwater Vehicle", *IEEE Access*, vol. 8, pp. 30119-30126, 2020, doi: 10.1109/ACCESS.2020.2972336.
- [4] S. Heshmati-Alamdari, A. Nikou and D. V. Dimarogonas, "Robust Trajectory Tracking Control for Underactuated Autonomous Underwater Vehicles in Uncertain Environments", *IEEE Transactions on Automation Science and Engineering*, vol. 18, no. 3, pp. 1288-1301, July 2021, doi: 10.1109/TASE.2020.3001183.
- [5] G. Antonelli, *Underwater Robots*, 3rd Edition, Springer Tracts in Advanced Robotics, Springer Cham, 2014, eBook ISBN: 978-3-319-37432-1. Published 27 August 2016. doi:10.1007/978-3-319-02877-4.

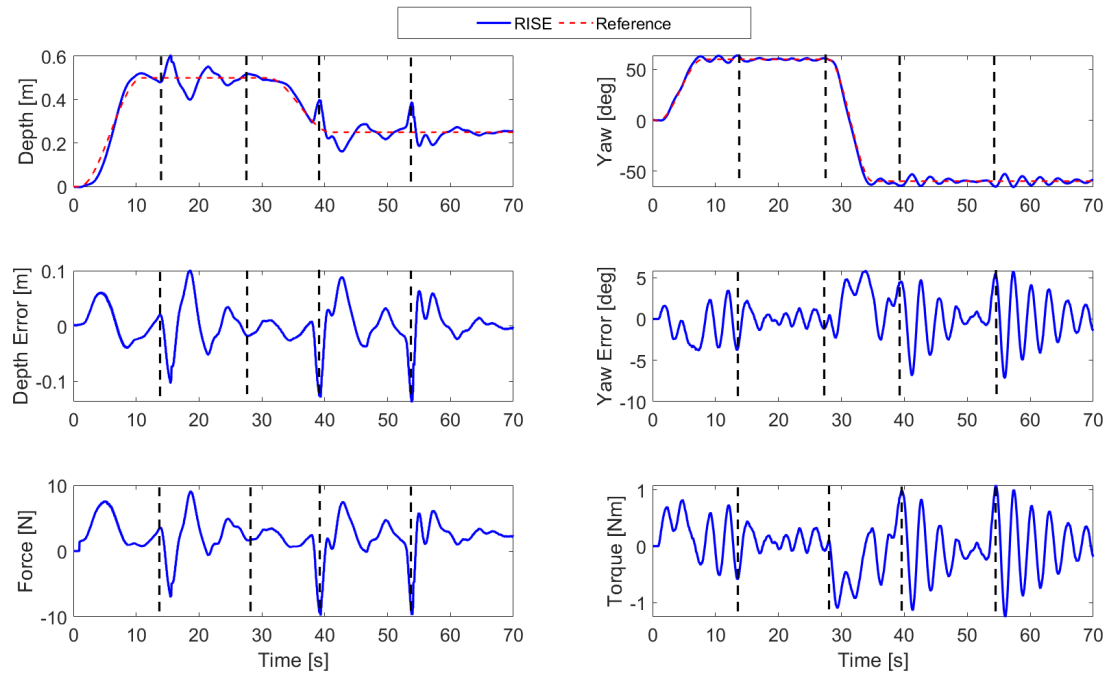


Figure 13: Robustness of the RISE controller towards external disturbances: (top graphs) tracking of depth and yaw, (middle graphs) corresponding tracking errors for depth and yaw, (bottom graphs) evolution versus time of the vehicle's control inputs.

[6] S. Zhao and J. Yuh, "Experimental study on advanced underwater robot control", *IEEE Transactions on Robotics*, vol. 21, no. 4, pp. 695-703, Aug. 2005, doi: 10.1109/TRO.2005.844682.

[7] T. Fossen, *Guidance and Control of Ocean Vehicles*, 1994.

[8] Qiang Chen, Tao Chen and Yong Zhang, "Research of GA-based PID for AUV motion control", 2009 International Conference on Mechatronics and Automation, Changchun, 2009, pp. 4446-4451, doi: 10.1109/ICMA.2009.5246715.

[9] D. Zhu, B. Sun, "The bio-inspired model based hybrid sliding-mode tracking control for unmanned underwater vehicles", *Engineering Applications of Artificial Intelligence*, vol.26, pp. 2260–2269, 2013, doi:10.1016/j.engappai.2013.08.017.

[10] A. S. Tijjani, A. Chemori and V. Creuze, "Robust Adaptive Tracking Control of Underwater Vehicles: Design, Stability Analysis, and Experiments", *IEEE/ASME Transactions on Mechatronics*, vol. 26, no. 2, pp. 897-907, April 2021, doi: 10.1109/TMECH.2020.3012502.

[11] X. Liu, X. Su, P. Shi and C. Shen, "Observer-Based Sliding Mode Control for Uncertain Fuzzy Systems via Event-Triggered Strategy", *IEEE Transactions on Fuzzy Systems*, vol. 27, no. 11, pp. 2190-2201, Nov. 2019, doi: 10.1109/TFUZZ.2019.2895804.

[12] W. Remmas, A. Chemori and M. Kruusmaa, "Diver Tracking in Open Waters: A Low-Cost Approach Based on Visual and Acoustic Sensor Fusion", *Journal of Field Robotics*, vol 38, no. 3, pp. 494-508, 2021, doi: 10.1002/rob.21999.

[13] I Eski, S. YILDIRIM, "Design of neural network control system for controlling trajectory of autonomous underwater vehicles", *International Journal of Advanced Robotic Systems*, vol. 11, pp 1–17, 2014, doi:10.5772/56740.

[14] D. Maalouf, A. Chemori, V. Creuze, "L1 adaptive depth and pitch control of an underwater vehicle with real-time experiments", *Ocean Engineering*, vol. 98, 2015, doi:10.1016/j.oceaneng.2015.02.002.

[15] J. Guerrero, J. Torres, V. Creuze, A. Chemori, "Trajectory tracking for autonomous underwater vehicle: An adaptive approach", *Ocean Engineering*, vol. 172, pp. 511–522, 2019, doi:10.1016/j.oceaneng.2018.12.027.

[16] C. Yu, X. Xiang, P. A. Wilson and Q. Zhang, "Guidance-Error-Based Robust Fuzzy Adaptive Control for Bottom Following of a Flight-Style AUV With Saturated Actuator Dynamics", *IEEE Transactions on Cybernetics*, vol. 50, no. 5, pp. 1887-1899, May 2020, doi: 10.1109/TCYB.2018.2890582.

[17] A. Tijjani, A. Chemori, V. Creuze, "A survey on tracking control of unmanned underwater vehicles: Experiments-based approach," *Annual Reviews in Control*, 2022, doi:10.1016/j.arcontrol.2022.07.001.

[18] B. Xian, D. M. Dawson, M. S. de Queiroz and J. Chen, "A continuous asymptotic tracking control strategy for uncertain nonlinear systems," in *IEEE Transactions on Automatic Control*, vol. 49, no. 7, pp. 1206-1211, July 2004, doi: 10.1109/TAC.2004.831148.

[19] N. Fischer, Z. Kan, R. Kamalapurkar and W. E. Dixon, "Saturated RISE Feedback Control for a Class of Second-Order Nonlinear Systems", *IEEE Transactions on Automatic Control*, vol. 59, no. 4, pp. 1094-1099, April 2014, doi: 10.1109/TAC.2013.2286913.

[20] N. Fischer, D. Hughes, P. Walters, E. M. Schwartz and W. E. Dixon, "Nonlinear RISE-Based Control of an Autonomous Underwater Vehicle", *IEEE Transactions on Robotics*, vol. 30, no. 4, pp. 845-852, Aug. 2014, doi: 10.1109/TRO.2014.2305791.

[21] A. S. Tijjani, A. Chemori, S. A. Ali and V. Creuze, "Continuous–Discrete Observation-Based Robust Tracking Control of Underwater Vehicles: Design, Stability Analysis, and Experiments", *IEEE Transactions on Control Systems Technology*, vol. 31, no. 4, pp. 1477-1492, July 2023, doi: 10.1109/TCST.2022.3224321.

[22] M. Taktak-Meziou, A. Chemori, J. Ghommam, N. Derbel, "A prediction-based optimal gain selection in RISE feedback control for hard disk drive", *IEEE Conference on Control Applications (CCA)*, pp. 2114–2119, Juan Les Antibes, France, 2014, doi: 10.1109/CCA.2014.6981615.

[23] T. Fossen, *Marine control systems: guidance, navigation and control of ships, rigs and underwater vehicles*, Vol. 28, 2002.

[24] J. Chen, H. Zhu, L. Zhang, Y. Sun, "Research on fuzzy control of path tracking for underwater vehicle based on genetic algorithm optimization", *Ocean Engineering*, vol. 156, pp. 217–223, 2018, doi:10.1016/j.oceaneng.2018.03.010.

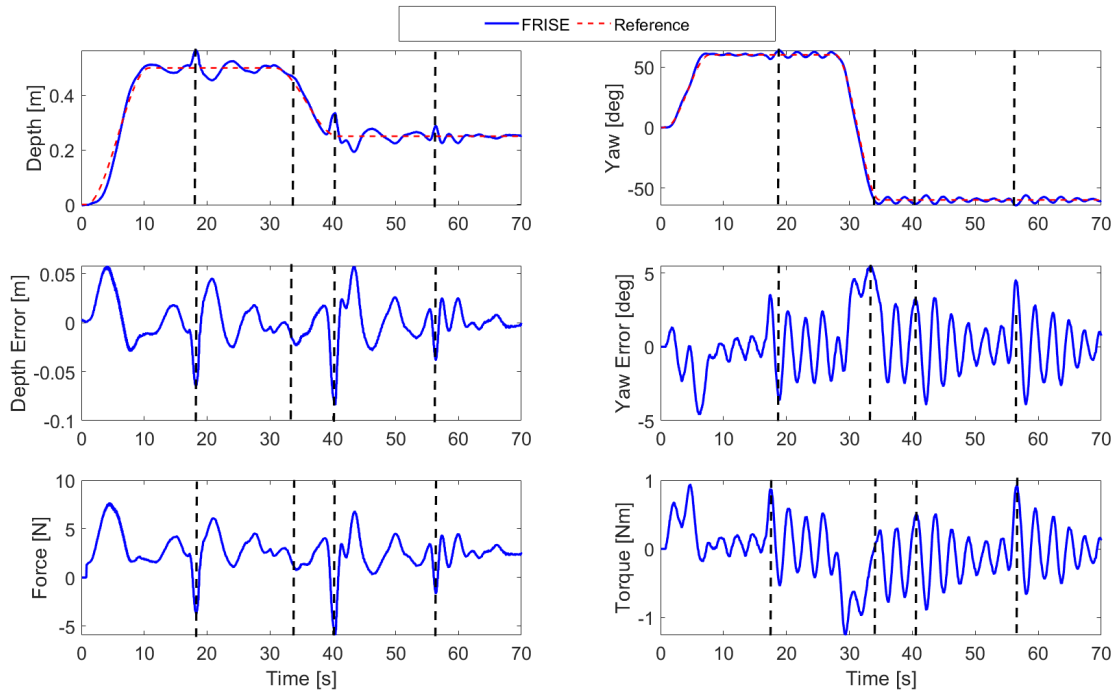


Figure 14: Robustness of the proposed FRISE controller towards external disturbances: (top graphs) tracking of depth and yaw, (middle graphs) corresponding tracking errors for depth and yaw, (bottom graphs) evolution versus time of the vehicle's control inputs.

- [25] C. Yu, X. Xiang, L. Lapierre, Q. Zhang, "Nonlinear guidance and fuzzy control for three-dimensional path following of an underactuated autonomous underwater vehicle", *Ocean Engineering*, vol. 146, pp. 457–467, 2017. doi:10.1016/j.oceaneng.2017.10.001.
- [26] J. M. Escorcia-Hernández, A. Chemori and H. Aguilar-Sierra, "Adaptive RISE Feedback Control for Robotized Machining With PKMs: Design and Real-Time Experiments", *IEEE Transactions on Control Systems Technology*, vol. 31, no. 1, pp. 39-54, Jan. 2023, doi: 10.1109/TCST.2022.3169015.
- [27] Y. Xie, A. Zhu, Z. Huang, "Research on the control performance of depth-fixed motion of underwater vehicle based on fuzzy-pid", *Journal of Robotics*, vol. 2023, pp. 1–10, 2023. doi:10.1155/2023/4168433.
- [28] X. Xiang, C. Yu, L. Lapierre, J. Zhang, Q. Zhang, "Survey on fuzzylogic-based guidance and control of marine surface vehicles and underwater vehicles", *International Journal of Fuzzy Systems*, vol. 20, pp. 572–586, 2018. doi:10.1007/s40815-017-0401-3.
- [29] E. Campos, A. Chemori, V. Creuze, J. Torres, R. Lozano, "Saturation based nonlinear depth and yaw control of underwater vehicles with stability analysis and real-time experiments", *Mechatronics*, vol. 45, pp. 49 – 59, 2017. doi:10.1016/j.mechatronics.2017.05.004.

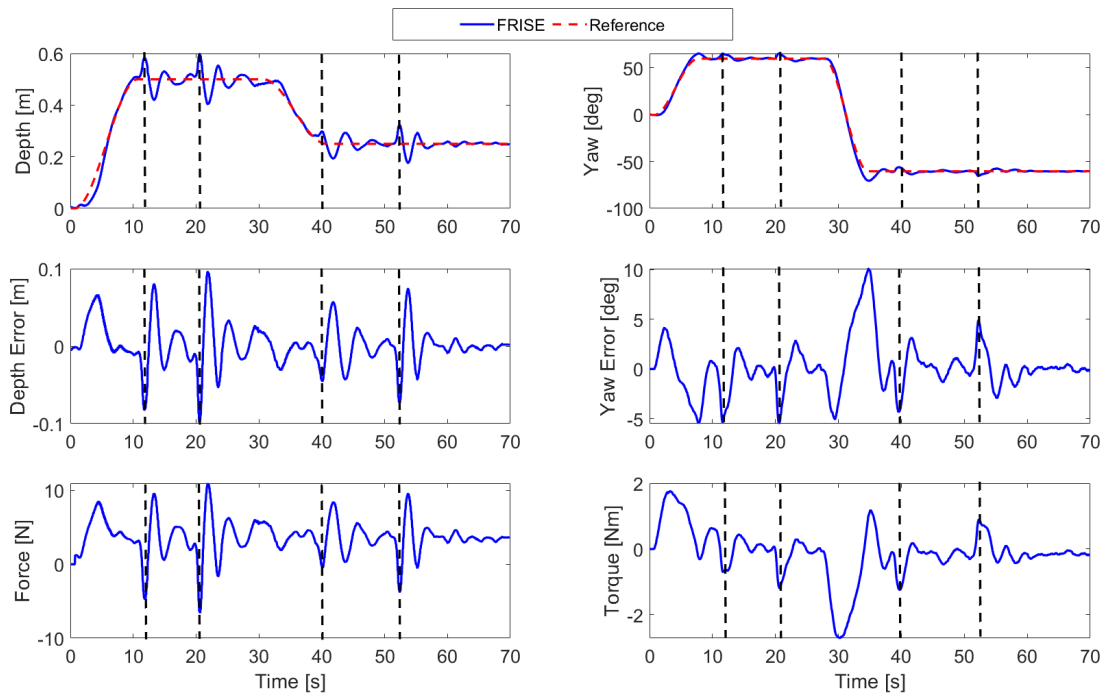


Figure 15: Robustness of the proposed FRISE controller towards external disturbances and parametric uncertainties: (top graphs) tracking of depth and yaw, (middle graphs) corresponding tracking errors for depth and yaw, (bottom graphs) evolution versus time of the vehicle's control inputs.